Received 29 March 2025, accepted 13 April 2025, date of publication 22 April 2025, date of current version 16 May 2025.

Digital Object Identifier 10.1109/ACCESS.2025.3563166

METHODS

Consistent Geometric Patterns Observed in Three-Dimensional Displacement of Nationwide GNSS Stations in Japan

JUNICHI SUSAKI, (Senior Member, IEEE)
Graduate School of Engineering, Kyoto University, Kyoto 615-8540, Japan
e-mail: susaki.junichi.3r@kyoto-u.ac.jp

This work was supported in part by the Grant-in-Aid for Scientific Research (KAKENHI) (C) under Grant 24K07712; in part by The Kajima Foundation, Japan; and in part by the Technical Research and Development for Road Policy Quality Improvement, the Ministry of Land, Infrastructure, Transport, and Tourism (MLIT), Japan.

ABSTRACT This study explored the possibility of using currently available data to forecast when and where a large earthquake could occur in the near future. Such forecasts require measurements and understanding of past and current three-dimensional (3D) displacement patterns. We analyzed the geometric patterns of 3D displacement using coordinate data from over 1,300 global navigation satellite system stations in Japan. We found that the monthly displacement velocities of a station were on a single flat plane, although a significantly large earthquake had occurred, and the normal planes of all stations were on a single quadratic curve surface. Moreover, the sum of the absolute differences in 15-d velocities indicated a significant displacement over a wide area after the occurrence of a large earthquake.

INDEX TERMS GNSS, 3D displacement, geometric pattern.

I. INTRODUCTION

Earthquakes are among the most destructive natural disasters worldwide in terms of casualties and damage to infrastructure. Japan has periodically experienced severe earthquakes. For example, the Great Hanshin Awaji earthquake, with a Japan Meteorological Agency magnitude scale of (Mj) 7.3, which occurred mainly in the Hyogo and Osaka prefectures on January 17, 1995 [1], [2], and the earthquake off the Pacific coast of Tohoku, at Mj 9.0, which occurred in eastern Japan on March 11, 2011 [3]. On January 1, 2024, the Noto Peninsula in central Japan was hit by a Mj 7.6 earthquake [4], [5]. An earthquake swarm was observed around this area, and the mechanism was analyzed and reported [6], [7], [8]. It has been reported that the main trigger of an earthquake is fluid flow in the crust [9], [10]. To mitigate the damage caused by severe earthquakes, it is essential to monitor land displacement on an operational basis and rapidly identify the signs of such an event, although this has not yet been accomplished successfully.

Monitoring of land displacement is conducted using remote sensing technology. Satellite-borne synthetic aperture radar (SAR) images are used widely to map land displacements. The interferometric SAR (InSAR) technique generates an interferogram image by determining the phase difference between two SAR images observed before and after an earthquake. The differential InSAR (DInSAR) technique measures land displacement by subtracting the elevation derived from an existing source from the estimated elevation. Further extensions using multitemporal SAR images and removing irrelevant noise, such as permanent scatterer InSAR (PSInSAR) [11], small baseline subset (SBAS) [12], and SqueeSAR [13] can achieve displacement velocities at millimeter-level accuracy [14].

The land displacement we obtained by SAR image analysis was along the line-of-sight (LOS) direction. Techniques for estimating three-dimensional (3D) displacement from two LOS displacements have been investigated. SAR images are observed in ascending or descending orbits; therefore, two

The associate editor coordinating the review of this manuscript and approving it for publication was Ayman El-Baz.

LOS displacements at a point of interest on the ground could be available. Pseudo-3D displacement is estimated by compensating for a lack of observations. For example, a 2.5-D analysis assumes that no north–south displacement occurs [15]. Two variables, the displacement velocities along the east–west and vertical directions, are estimated from two LOS observations. This assumption is based on SAR observations being nearly along an east–west direction; therefore, they are less sensitive to displacement along the north–south direction than those along other directions. This approach could generate an approximate 3D displacement and is effective under the limitation that no data other than SAR images are available. However, this approach, with an unreasonable assumption, includes bias in the estimated 3D land displacements.

Light detection and ranging (LiDAR) can rapidly measure surface height and generate accurate coordinate data of the surface. Using airborne LiDAR is popular; however, the aircraft platform has a serious limitation in that a wide area cannot be covered at acceptable cost. This platform is not suitable for operational monitoring, although it is now used widely for emergency cases immediately after the occurrence of natural disasters that cause critical damage. Apart from aircraft, several space agencies have already used or intend using other platforms. The US National Aeronautics and Space Administration (NASA) operates a LiDAR onboard the International Space Station (ISS), namely the Global Ecosystem Dynamics Investigation (GEDI) [16]. The Japan Aerospace Exploration Agency (JAXA) is preparing the installation of a LiDAR, namely a Multi-Sensing Observation Lidar and Imager Demonstration (MOLI). The aims of MOLI is mainly the monitoring of forest heights to understand biomass [17]. Both GEDI and MOLI have limitations as their swaths are narrow. For example, the GEDI swath is equivalent to 5.4 km [18]. Moreover, the observation is basically at a nadir from the orbits of the ISS; therefore, it takes several months to cover a wide area. Several LiDAR onboard satellites have been launched, e.g., NASA has launched the Ice, Cloud, and Land Elevation Satellite (ICESat) [19] for terrestrial missions, and ICESat-2 [20] for glacier monitoring. More satellite-borne LiDARs are expected to be launched but high accuracy of airborne LiDAR is not anticipated.

Another traditional data source for 3D land displacement is a Global Navigation Satellite System (GNSS) deployed on the ground. Networking is key to GNSS observations for removing errors and achieving highly accurate coordinates. The International GNSS Service (IGS) [21] is an example of an international GNSS network. In the United States, the National Geodetic Survey (NGS), a division of the National Oceanic and Atmospheric Administration (NOAA), manages the NOAA Continuously Operating Reference Station (CORS) Network (NCN). This network includes more than 1,000 GNSS stations in the United States [22]. In Europe, the Regional Reference Frame Sub-Commission for Europe (EUREF) Permanent GNSS Network has 420 GNSS stations [23], [24]. In Spain, Network of GNSS Permanent Stations of Spain (ERGNSS) operates more than 120 GNSS stations [25]. In Germany, the Helmholtz Centre for Geosciences operates a global GNSS station network, comprising approximately 70 stations [26].

In Japan, the Geospatial Authority of Japan (GSI) has deployed over 1,300 GNSS stations, and the processed 3D geolocational data are available to the public. This system is known as the GNSS Earth Observation Network System (GEONET) [27], [28]. These collected data have been used to understand the mechanisms of land displacement and deformation [29], [30], [31], [32]. Although the data are accurate, they are spatially sparse. The stations are approximately 20 km apart. GNSS data are often used to combine SAR-derived displacements to estimate 3D land displacements. Because GNSS data are spatially sparse, geostatistical interpolation techniques such as kriging can be applied to generate 3D data at points of interest [33], [34], [35]. However, this technique has a critical issue because the interpolated displacement could be inconsistent with the actual displacement. This is often the case when a local displacement feature is observed that differs from the displacement trend in the area of interest. The interpolation could fail to detect such a local displacement; therefore, the final 3D displacement could be erroneous [36], [37]. A technique to detect inconsistencies between interpolated GNSS data and SAR observations has been proposed to avoid errors in 3D displacement [37].

Regarding wide areas of interest, e.g., at national or continental level, the spatial sparsity of the GNSS data network is not important, and GNSS data could be appropriate for estimating 3D displacement. Temporal GNSS data can support an analysis of an earthquake mechanism. The analysis requires data measured before and after the earthquake. However, understanding the long-term land displacement mechanism at a national scale and deriving a specific indicator to forecast significantly large displacements are still lacking. In the current study, we investigated GNSS coordinate data to determine pointers to facilitate understanding of the land displacement mechanism.

II. DATA USED

We downloaded GEONET data for the period 2017–2024 from the GSI website [38]. The analysis to fix the station coordinates comprises two steps, namely reference station analysis (RSA) and GEONET station analysis (GSA) [28]. The current system, which began in April 2021, releases three types of coordinate products, namely F5, R5, and Q5. Although F5 is the name of the current system, it represents one of the coordinate products. F5 and R5 are the final and rapid-coordinate products, respectively. Q5 is an ultra-rapid product. The root mean square (RMS) averaged over all GEONET stations indicated extremely high accuracy of 3.2 mm (horizontal) and 7.3 mm (vertical). In this study, we downloaded and used the daily F5 coordinates from GEONET stations since 2017 [38].

III. RESULTS

A. EXPERIMENTAL DESIGN

We aimed to examine a priori features to forecast a significantly large earthquake from temporal coordinates observed by GNSS stations. We started with a nationwide visualization of annual displacement velocities in Japan. Subsequently, we focused on the geometric patterns formed by the displacement velocities at each GNSS station. Afterward, we investigated the meaning of the geometric patterns common to the entire GNSS station by fitting the geometric surface. Finally, a metric was derived to understand the displacement from the obtained results.

B. VELOCITIES FROM COORDINATES

It is often the case that the original coordinates are converted into the relative coordinates to a specific GNSS station for land displacement analysis to remove errors caused by local climate change, ionosphere disturbance or other factors. In this research, we calculated the relative coordinates against a GNSS station "Tsukuba 1" that is one of the most commonly used stations for such purpose. The latitude and longitude of the station were 36.10611 and 140.08721, respectively as of January 1, 2025. Because the coordinates fluctuated significantly, we applied a 15-d moving average filter. We selected the duration of the moving average as 15-d as it was the most effective in removing noise and preventing the loss of temporal change data stemming from over-smoothing. The averaged coordinates in the east–west, north–south, and vertical directions were obtained.

Figures 1, 2, and 3 show the displacement velocities along the east–west, north–south, and vertical directions, respectively. These were obtained from the coordinates of the GNSS stations after applying a 15-d moving average filter. The duration of the calculation for each panel was one year.

Figure 4(a), 4(b), and 4(c) shows the temporal changes in displacement along the east–west, north–south, and vertical directions at the Sadohara Station, Miyazaki Prefecture. The geolocation is indicated by S1 in Fig. 1(g), 2(g), and 3(g). This area was affected by a significantly large earthquake of Mj 7.1 on August 8, 2024. Hereafter, we refer to this area as Station 1. Figure 4(a) and 4(b) shows a large displacement along the south–east direction, whereas Fig. 4(c) shows that periodic subsidence occurred before the earthquake. Similarly, Figs. 4(d), 4(e), and 5(f) show the temporal changes in displacement along the east–west, north–south, and vertical directions at Suzu Station, Ishikawa Prefecture. These changes are indicated by S2 in Fig. 1(g), 2(g), and 3(g). On January 1, 2024, an earthquake (Mj 7.6) occurred near this area. Hereafter, we refer to this area as Station 2. Figure 4(d), 4(e), and 4(f) clearly shows that displacements of a few meters occurred at this station.

C. PLANAR SURFACE ESTIMATION

We estimated the planar surface from a certain velocity period for a GNSS station. The planar surface parameters were obtained by minimizing the sum of the distances between the velocities and planar surface.

$$aV_E + bV_N + cV_U + d = 0 \tag{1}$$

where a, b, and c represent coefficients of velocities along east–west, north–south, and vertical directions, respectively and $a^2 + b^2 + c^2 = 1$.

The optimal parameters $\left(\hat{a}, \hat{b}, \hat{c}, \hat{d}\right)$ can be estimated by solving (2):

$$\begin{aligned} &\arg\min \sum r_i^2 \\ &= \arg\min \sum \left(aV_{E,i} + bV_{N,i} + cV_{U,i} + d\right)^2 \end{aligned} \tag{2}$$

where r_i is the distance between a point $(V_{E,i}, V_{N,i}, V_{U,i})$ and the planar surface. The minimum eigenvalue, and thus the minimum eigenvector, of the matrix (3), as shown at the bottom of the next page, were calculated where $\bar{V}_E$, $\bar{V}_N$, and $\bar{V}_U$ are the means of V_E, V_N, and V_U, respectively. The minimum eigenvector is equivalent to the optimal parameters $\left(\hat{a}, \hat{b}, \hat{c}\right)$.

Figure 5 shows the monthly displacement velocity of Stations 1 and 2 as points in the 3D coordinate system in the east–west, north–south, and vertical directions. Each point was tracked from month to month. The planar surface area was estimated for each year using these velocities. Figure 5(a)–5(g) shows the displacement velocities and estimated planar surfaces from 2018 to 2024 at Station 1, respectively. We estimated a single planar surface at Station 1 for all the monthly velocities from 2017 to 2024, as shown in Fig. 5(h). The equation for the planar surface shown in Fig. 5(h) is:

$$0.7758V_E + 0.5727V_N - 0.2650V_U - 0.0045 = 0 \tag{4}$$

The root mean square error (RMSE) for Fig. 5(h) was 0.010 m/year. We repeated the same process with data from Station 2. The results are shown in Fig. 5(i)–5(p). The equation for the planar surface shown in Fig. 5(p) is:

$$0.5339V_E + 0.7888V_N - 0.3044V_U = 0 \tag{5}$$

The RMSE for Fig. 5(p) was 0.009 m/year.

D. PLANAR NORMAL SCATTERING AND CURVE SURFACE FITTING

Figure 6 shows that three components of the normal of a planar surface (a, b, c) are scattered in the 3D coordinate system. Here, a, b, and c represent coefficients of velocities along the east–west, north–south, and vertical directions, respectively. The results of each year are shown in two panels, e.g., Fig. 6(a) and 6(b), 6(c) and 6(d), from different viewpoints.

The parameters of the normal planar surface (a, b, c) were plotted into a three-dimensional coordinate system. Figure 7 shows the results of a curve surface fitting for the two cases, the normal coefficients and monthly displacement velocities.

The optimal parameters of a curve surface fitting, $\hat{\beta}_o, \cdots, \hat{\beta}_5$ were estimated by solving (6):

$$\arg\min \sum \left(c_i - (\beta_o + \beta_1 a_i + \beta_2 b_i + \beta_3 a_i^2 + \beta_4 a_i b_i + \beta_5 b_i^2)\right)^2 \tag{6}$$

Figure 7(a) and 7(b) shows the results of fitting a curve surface to the normal coefficients (a, b, and c) obtained from the coordinates observed from 2017 to 2024. Figure 7(a) and 7(b) shares the same results, but have different viewpoints. The estimated curve surface equations for Fig. 7(a) and 7(b) are:

$$c = 0.4309 - 2.7278\,a - 3.6426b + 2.4672a^2 + 2.2414ab + 3.1326b^2 (R^2 = 0.9862) \tag{7}$$

where R^2 denotes the coefficient of determination for curve surface fitting. The RMSE was 0.0056 m/year. Note that we excluded outliers of (a, b, c) obtained. The exclusion was based on the points being far away from the population of other points in the feature space of (a, b, c). The thresholds for outliers were set as $b < 0.2$ or $c > 0.5$. The number of samples were reduced from 1, 246 to 1,199.

Figure 7(c) and 7(d) shows the results of fitting a curve surface to the monthly displacement velocities obtained from coordinates observed from 2017 to 2024. The estimated curve surface equations for Fig. 7(c) and 7(d) are:

$$V_U = -0.0074 + 1.4433V_E + 1.6581V_N + 1.8706V_E^2 + 4.7791V_E V_N + 2.0771V_N^2 (R^2 = 0.7469) \tag{8}$$

where V_E, $V_{N,}$ and V_U denote the velocities along the east–west, north–south, and vertical directions, respectively. The RMSE was 0.0296 m/year. Note that we also excluded outliers of (V_E, V_N, V_U) obtained. The thresholds for outliers were set as $|V_E| > 1.0$, $|V_N| > 1.0$ or $|V_U| > 1.0$. The number of samples were reduced from 125,400 (=1,320×(8 years ×12 months – 1)) to 122,993.

E. DERIVATIVE OF VELOCITIES

We calculated the sum of the absolute derivatives of velocities for each GNSS station. We calculated the absolute difference in velocities and divided it by time in years. The obtained results were equivalent to the acceleration of displacement in m/year^2. In this calculation, we initially used the monthly velocities. After this examination, we increased the temporal resolution from monthly to an interval of 15 d. This interval was chosen because we found that the derivative of velocities expressed more temporal changes than those based on other intervals, such as monthly intervals. In addition, we shortened the calculation duration from one year to one month. This one-month period was effective for understanding nationwide motions and local differences. The selected results of the sum of the absolute derivatives of velocities from the 2017 to 2024 are shown in Fig. 8.

F. ADDITIONAL ANALYSIS OF DATA OBTAINED DURING ANOTHER PERIOD

To confirm the validity of these results, we repeated the same processing of the data obtained for 2009–2016. Figure 9 shows the results of fitting a curve surface to the normal coefficients (a, b, and c) obtained from the coordinates observed for 2017–2024. We calculated the annual figures without excluding any data. The estimated curve surface equations for Fig. 9(a) and 9(b) are:

$$c = -0.3817 - 0.8765\,a - 2.2359b + 1.5582a^2 + 0.8055ab + 2.4492b^2 (R^2 = 0.9611) \tag{9}$$

The RMSE was 0.015 m/year. We also calculated the sum of the absolute derivatives of velocities from 15-d velocities every six months. The selected results of the sum of the absolute derivatives of the velocities from 2009 to 2016 are shown in Fig. 10.

IV. DISCUSSION

A. PLANAR SURFACE FROM VELOCITIES AT GNSS STATIONS

A1, indicated by a circle in Fig. 3(a), includes Miyagi Prefecture, and shows a much larger uplift than that of neighboring areas. Miyagi Prefecture was most severely damaged by the 2011 Tohoku earthquake. The A1 area shows unique displacement in both the east–west and north–south directions. Displacement or displacement velocities are suitable for pointing out areas that exhibit extremely large displacements; however, no other clues were inferred.

Interestingly, the displacement velocities were scattered on a planar surface, as shown in Figs. 6 and 7. In almost all instances, although a significantly large displacement occurred, the displacement velocities remained close to those of the same planar surface. S1 and S2 were hit by large earthquakes on August 8 and January 1, 2024, respectively. The severity of the earthquakes is supported by the sharp displacement shown in Fig. 4. Figure 5 indicates that in each year, the displacement velocities were on a planar surface, and their normal values differed slightly from each other. However, Fig. 5(h) and 5(p) shows that the velocities from 2017 to 2024 in S1 and S2 were plotted for each planar surface, with acceptable RMSE of 0.010 and 0.009 m/year, respectively.

$$\begin{pmatrix} \sum (V_{E,i} - \bar{V}_E)^2 & \sum (V_{E,i} - \bar{V}_E)(V_{N,i} - \bar{V}_N) & \sum (V_{E,i} - \bar{V}_E)(V_{U,i} - \bar{V}_U) \\ \sum (V_{E,i} - \bar{V}_E)(V_{N,i} - \bar{V}_N) & \sum (V_{N,i} - \bar{V}_N)^2 & \sum (V_{N,i} - \bar{V}_N)(V_{U,i} - \bar{V}_U) \\ \sum (V_{E,i} - \bar{V}_E)(V_{U,i} - \bar{V}_U) & \sum (V_{N,i} - \bar{V}_N)(V_{U,i} - \bar{V}_U) & \sum (V_{U,i} - \bar{V}_U)^2 \end{pmatrix} \tag{3}$$

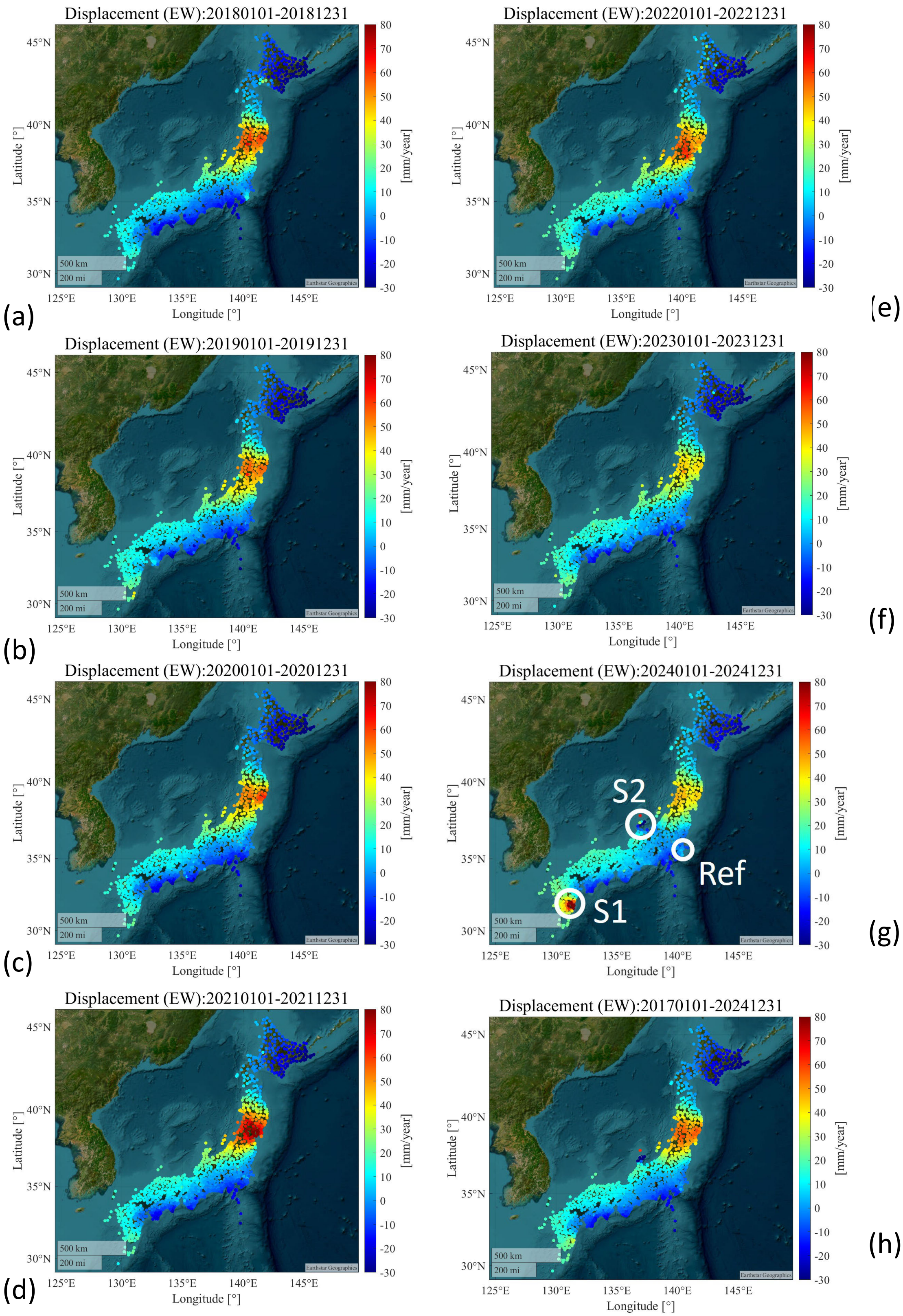

FIGURE 1. Annual displacement velocity along the east–west direction in Japan. Results are for (a) 2018, (b) 2019, (c) 2020, (d) 2021, (e) 2022, (f) 2023, (g) 2024, and (h) 2017–2024. S1 and S2 denote the GNSS stations Sadohara, Miyazaki Prefecture, and Suzu, Ishikawa Prefecture, respectively. Ref denotes a reference GNSS station, "Tsukuba 1" to calculate a relative displacement.

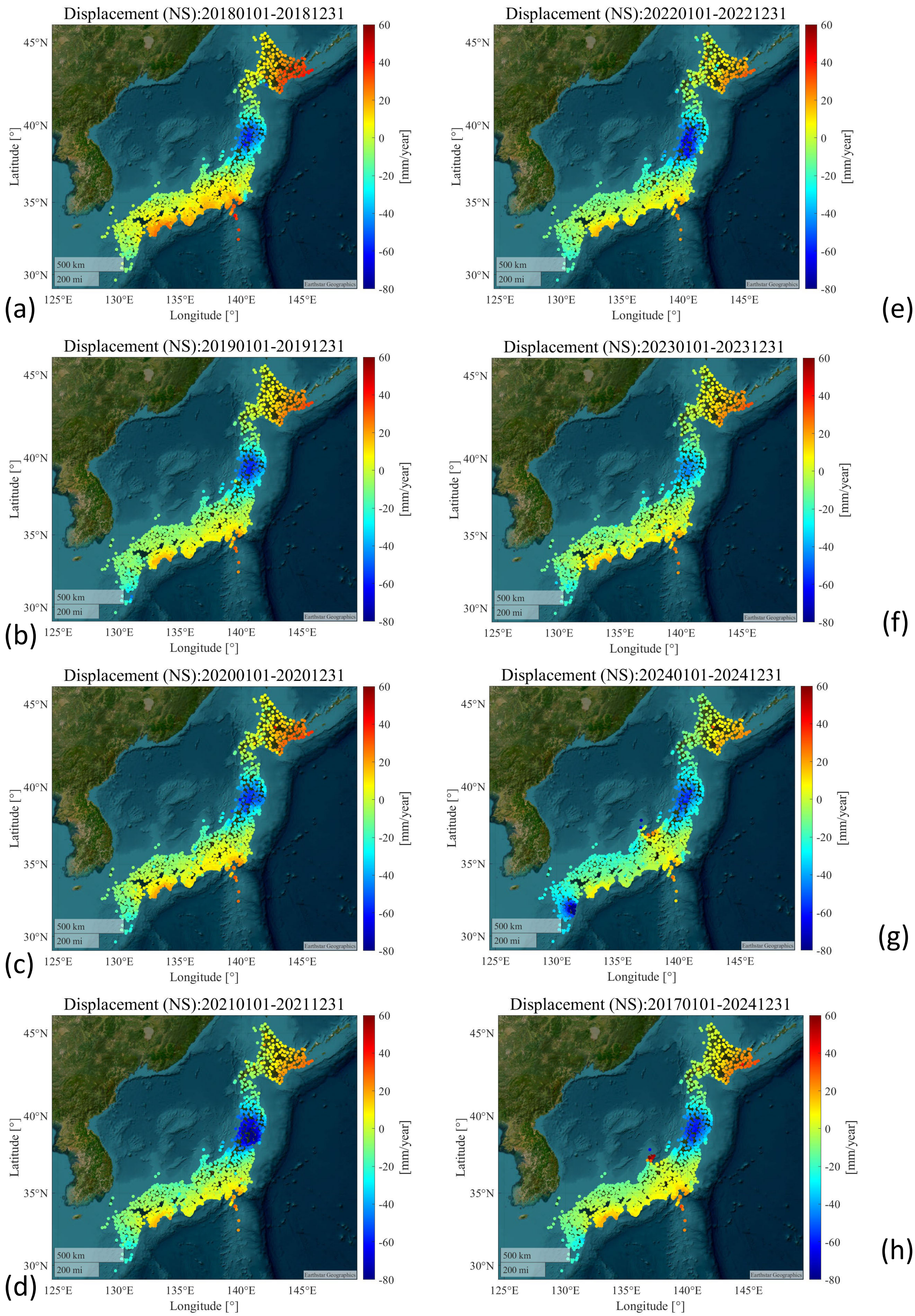

FIGURE 2. Annual displacement velocity along the north–south direction in Japan. Results are for (a) 2018, (b) 2019, (c) 2020, (d) 2021, (e) 2022, (f) 2023, (g) 2024, and (h) 2017–2024.

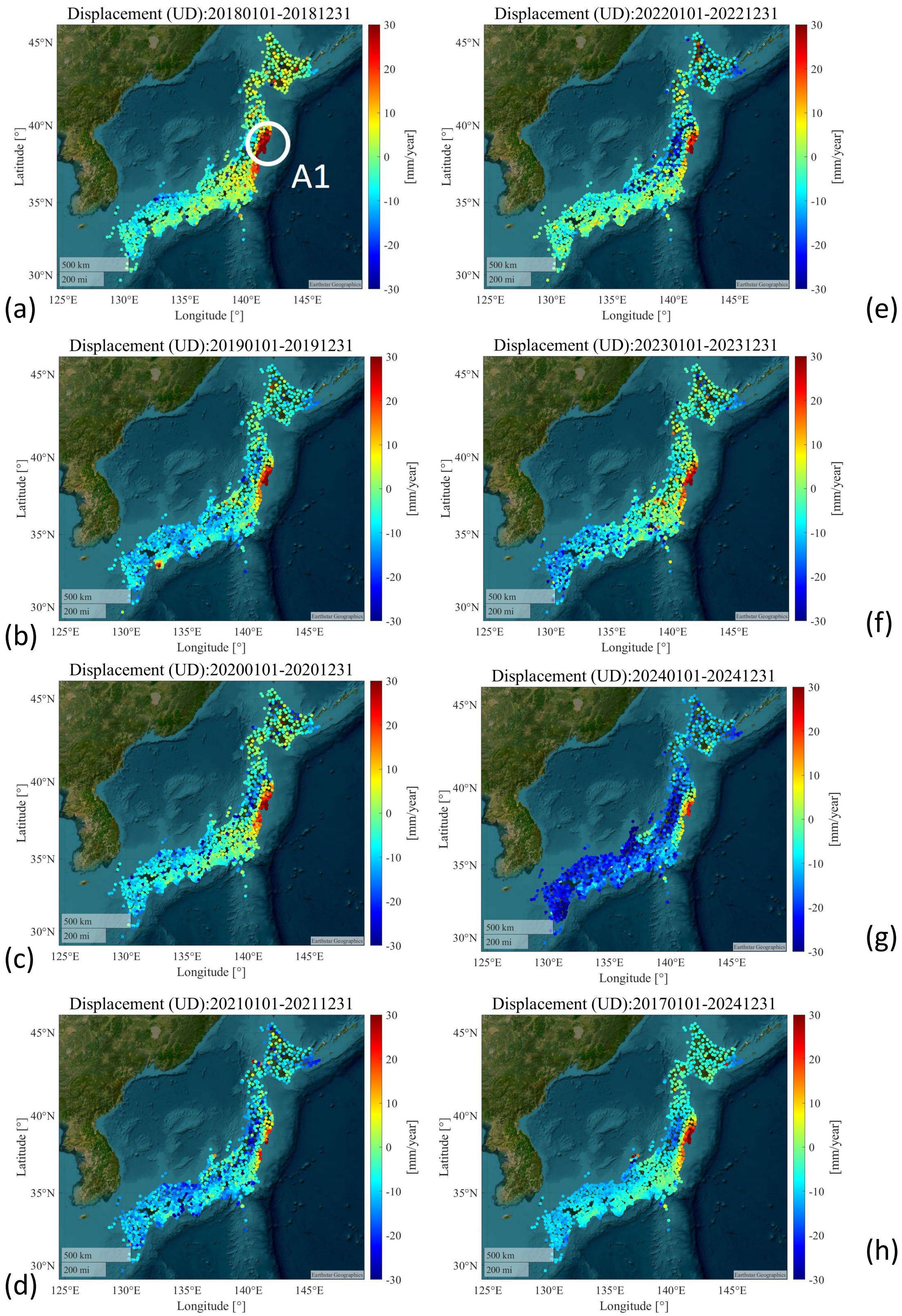

FIGURE 3. Annual displacement velocity along the vertical direction in Japan. Results are for (a) 2018, (b) 2019, (c) 2020, (d) 2021, (e) 2022, (f) 2023, (g) 2024, and (h) 2017–2024. A1 denotes the Miyagi Prefecture.

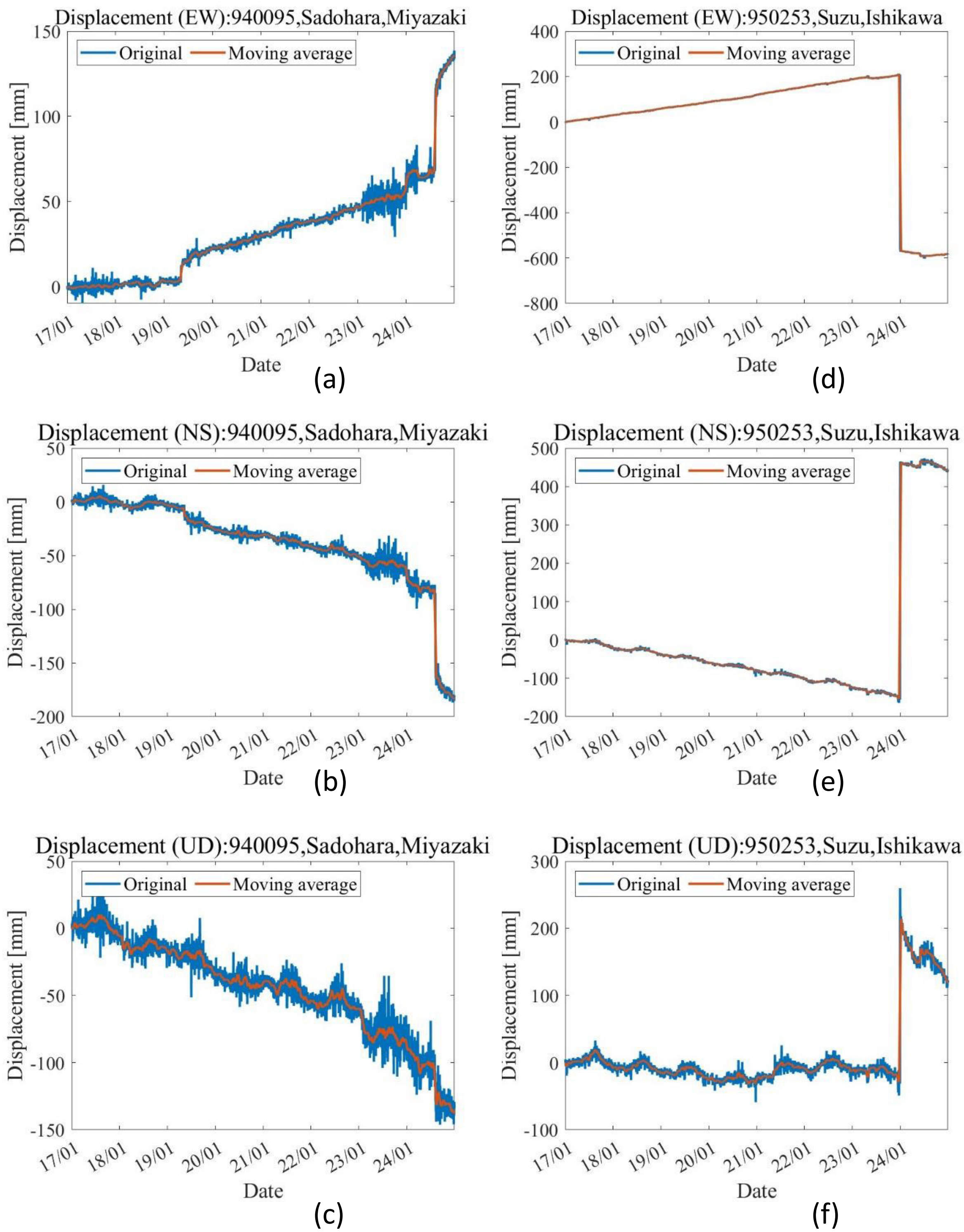

FIGURE 4. Temporal change of displacement along the east–west, north–south, and vertical directions. Results are along (a) east–west, (b) north–south, and (c) vertical directions in Sadohara, Miyazaki Prefecture (S1), respectively. Results are along (d) east–west, (e) north–south, and (f) vertical directions in Suzu, Ishikawa Prefecture (S2), respectively. Blue and red solid lines denote original coordinates and 15-d moving averaging filtered coordinates, respectively.

This finding indicates that although the displacement and monthly displacement velocities exhibit randomness, they follow a type of regulation in which the velocities remain on the same planar surface.

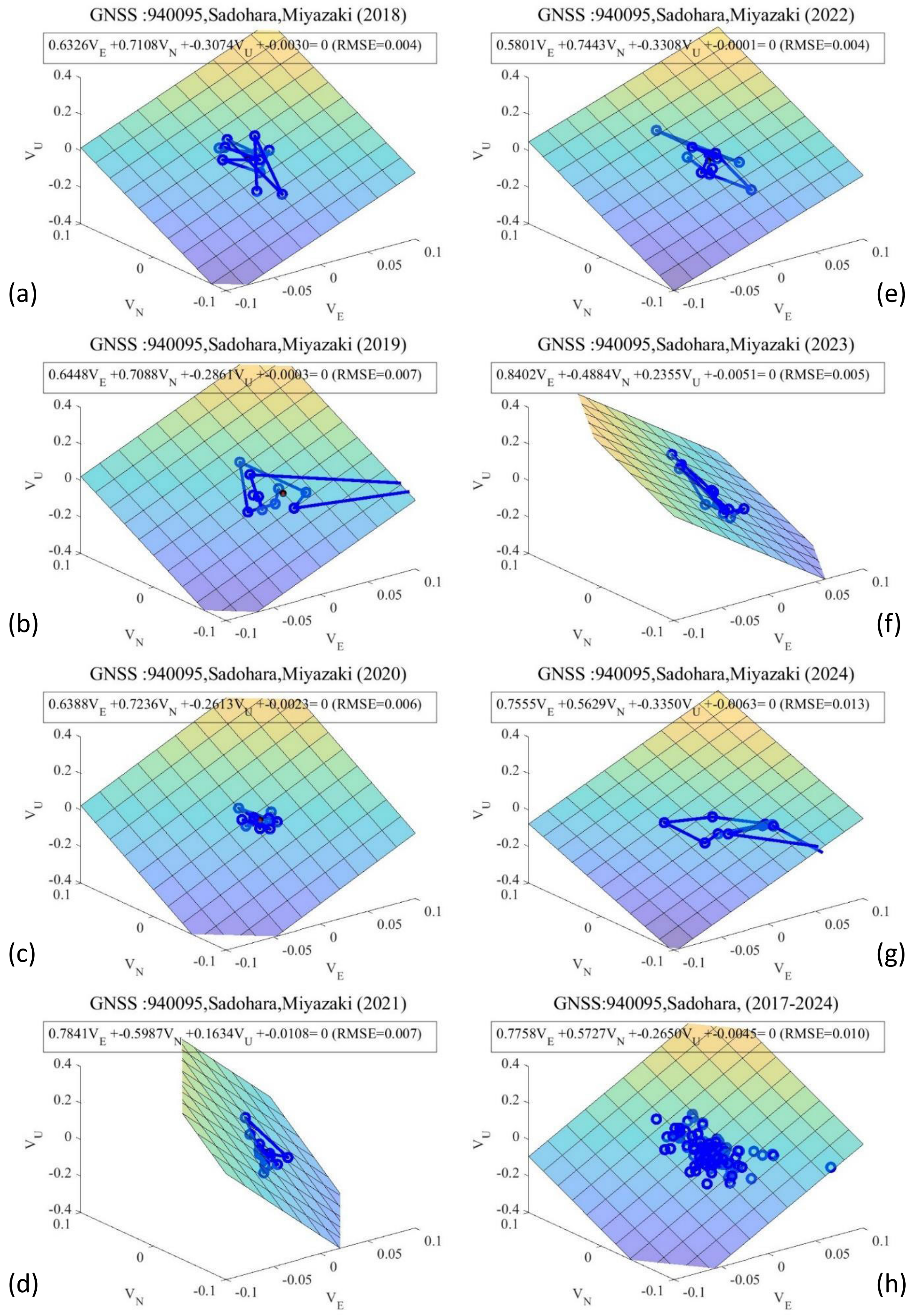

FIGURE 5. Monthly displacement velocity plots and fitted planar surface in Sadohara, Miyazaki Prefecture (S1) for (a) to (h) and in Suzu, Ishikawa Prefecture (S2) for (i) to (p). Results are obtained by using coordinates in (a,i) 2018, (b,j) 2019, (c,k) 2020, (d,l) 2021, (e,m) 2022, (f,n) 2023, (g,o) 2024, and (h,p) 2017– 2024. Regarding (a) to (g) and (j) to (o), time-series monthly displacements are connected with lines. Red points in (a) to (g) and (j) to (o) denote centroid of velocity plots in each year.

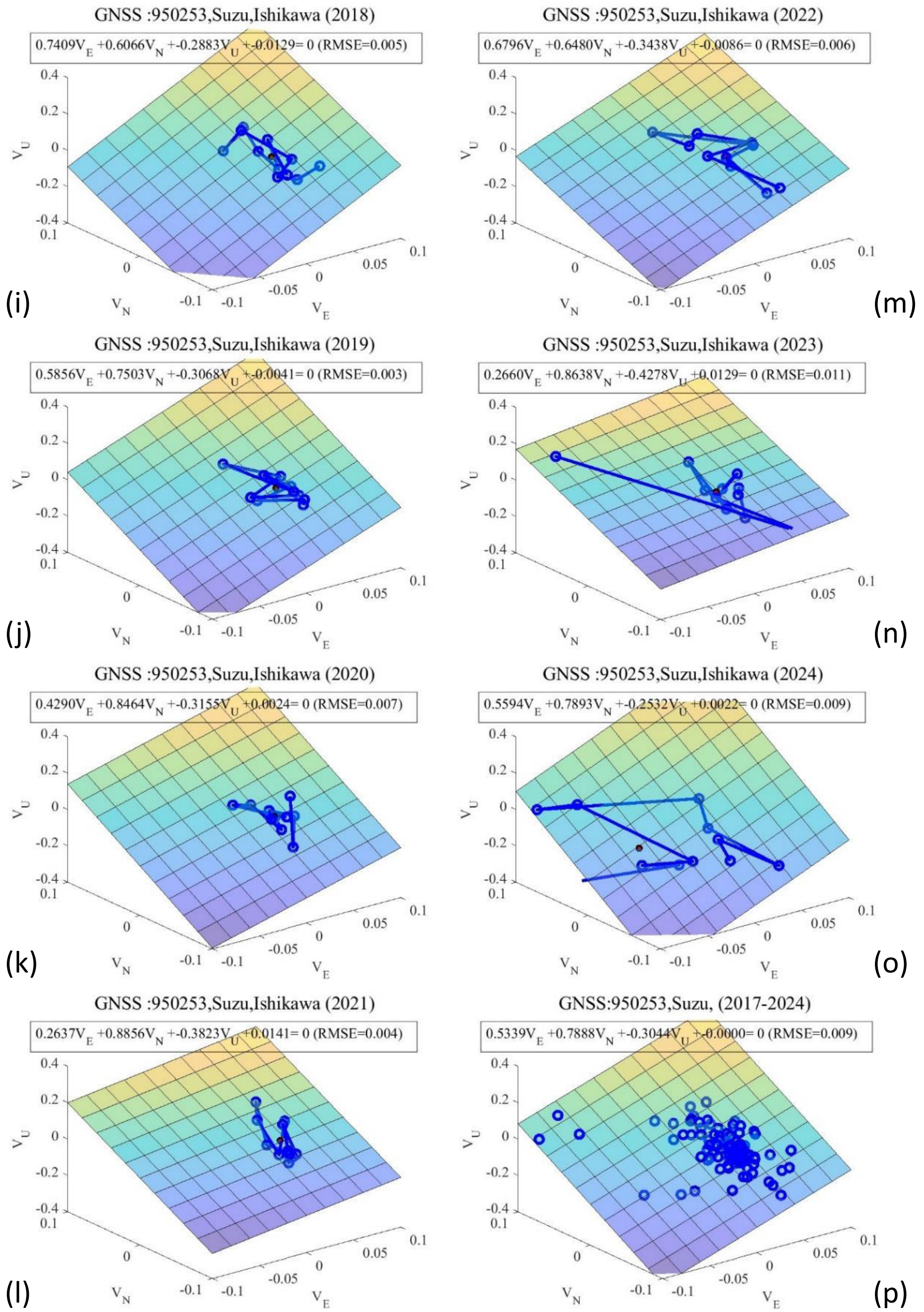

FIGURE 5. *(Continued.)* **Monthly displacement velocity plots and fitted planar surface in Sadohara, Miyazaki Prefecture (S1) for (a) to (h) and in Suzu, Ishikawa Prefecture (S2) for (i) to (p). Results are obtained by using coordinates in (a,i) 2018, (b,j) 2019, (c,k) 2020, (d,l) 2021, (e,m) 2022, (f,n) 2023, (g,o) 2024, and (h,p) 2017– 2024. Regarding (a) to (g) and (j) to (o), time-series monthly displacements are connected with lines. Red points in (a) to (g) and (j) to (o) denote centroid of velocity plots in each year.**

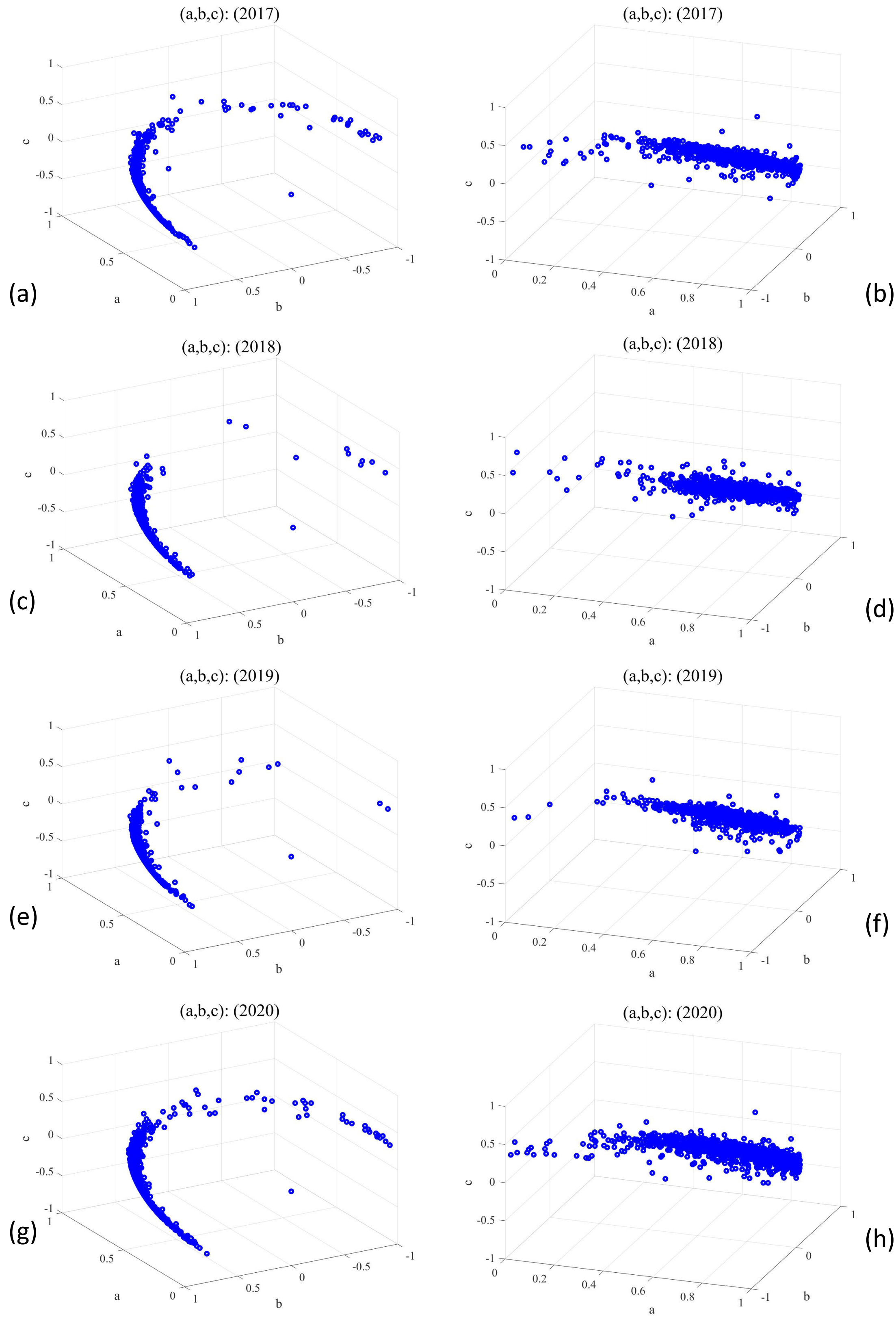

FIGURE 6. Scattering of normal of planar surface. 'a', 'b', and 'c' represent coefficients of velocities along the east–west, north–south, and vertical directions, respectively. Results are obtained by using coordinates in (a,b) 2017, (c,d) 2018, (e,f) 2019, (g,h) 2020, (I,j) 2021, (k,l) 2022, (m,n) 2023, and (o,p) 2024. For example, 8(a) and 8(b) share the same results from different viewpoints.

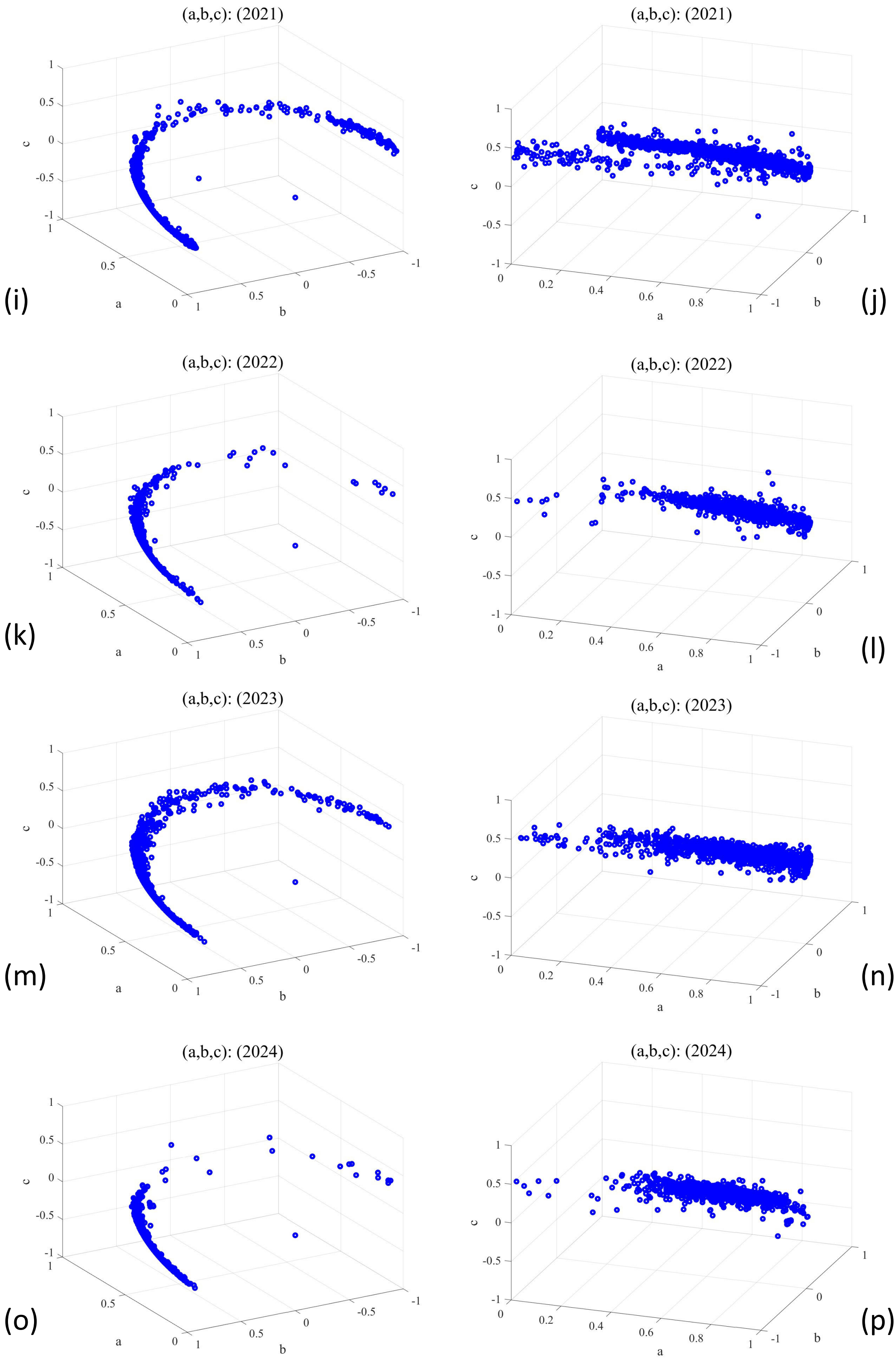

FIGURE 6. *(Continued.)* **Scattering of normal of planar surface. 'a', 'b', and 'c' represent coefficients of velocities along the east–west, north–south, and vertical directions, respectively. Results are obtained by using coordinates in (a,b) 2017, (c,d) 2018, (e,f) 2019, (g,h) 2020, (I,j) 2021, (k,l) 2022, (m,n) 2023, and (o,p) 2024. For example, 8(a) and 8(b) share the same results from different viewpoints.**

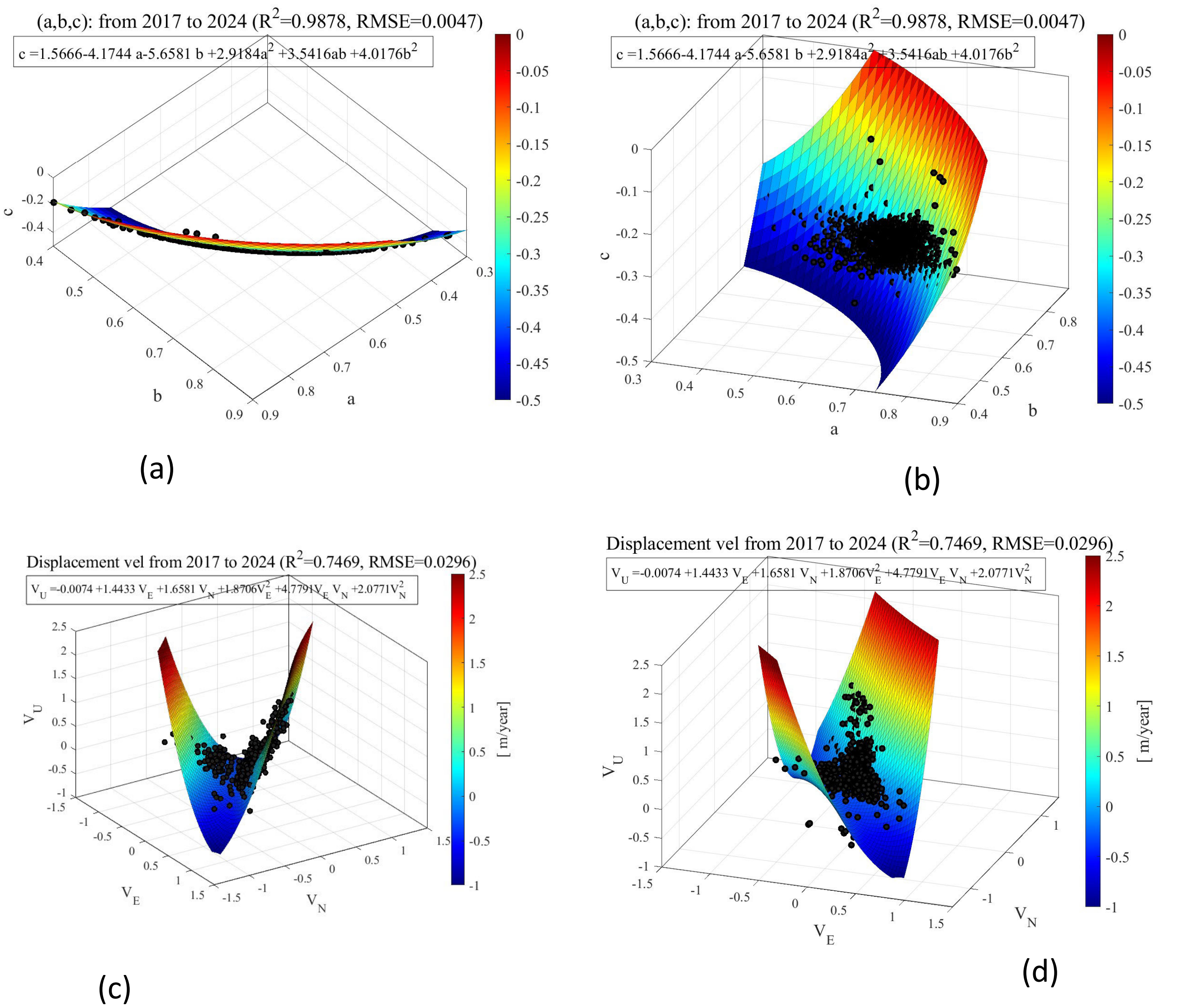

FIGURE 7. Curve surface fitting results. Results are obtained by fitting to (a,b) normal coefficients (a, b, c) obtained from the coordinates for 2017–2024, and (c,d) monthly displacement velocities obtained from coordinates observed for 2017–2024. The coefficients of determination in curve surface fitting are 0.9862 for (a,b) and 0.7469 for (c,d), respectively.

B. PLANAR NORMAL SCATTERING FEATURE

An interesting point is that the normal components (a, b, c) of the planar surfaces form a quadratic curve surface, as expressed by (8). As shown in Fig. 7, quadratic curve surface fitting achieved a significantly high coefficient of determination, R2 = 0.9862. Figure 6(a), 6(c), 6(e), 6(g), 6(i), 6(k), 6(m), and 6(o) supports this conclusion. Additionally, the scattergrams of (a, b, c) repeated convergence and divergence periodically, as shown in Fig. 6(g), 6(i), 6(k), 6(m), and 6(o). We assumed that such a move could be an indicator of significant displacement, i.e., an earthquake, and investigated the temporal changes in (a, b, c). However, attempts to derive a meaningful indicator from the temporal changes in (a, b, c) were unsuccessful. This factor should be examined further in future studies.

Regarding the displacement velocities shown in Fig. 7(c) and 7(d), fitting a quadratic curve surface was not successful, with a coefficient of determination of R2 = 0.7469. Figure 7(c) shows a scattergram of the velocities of the two streams, and Fig. 7(c) and 7(d) show that the distances to the curve surface were not as small as those in Fig. 7(a) and 7(b). The displacement velocity could potentially easily explain the physical meaning of occurrences both on and under the surface. However, the current results do not provide such information.

C. TEMPORAL CHANGE OF DERIVATIVE OF VELOCITIES

Based on the aforementioned results and discussion, we focused on the derivatives of velocities. From a physics viewpoint, the derivative denotes the acceleration of the coordinates. We did not consider the positive or negative

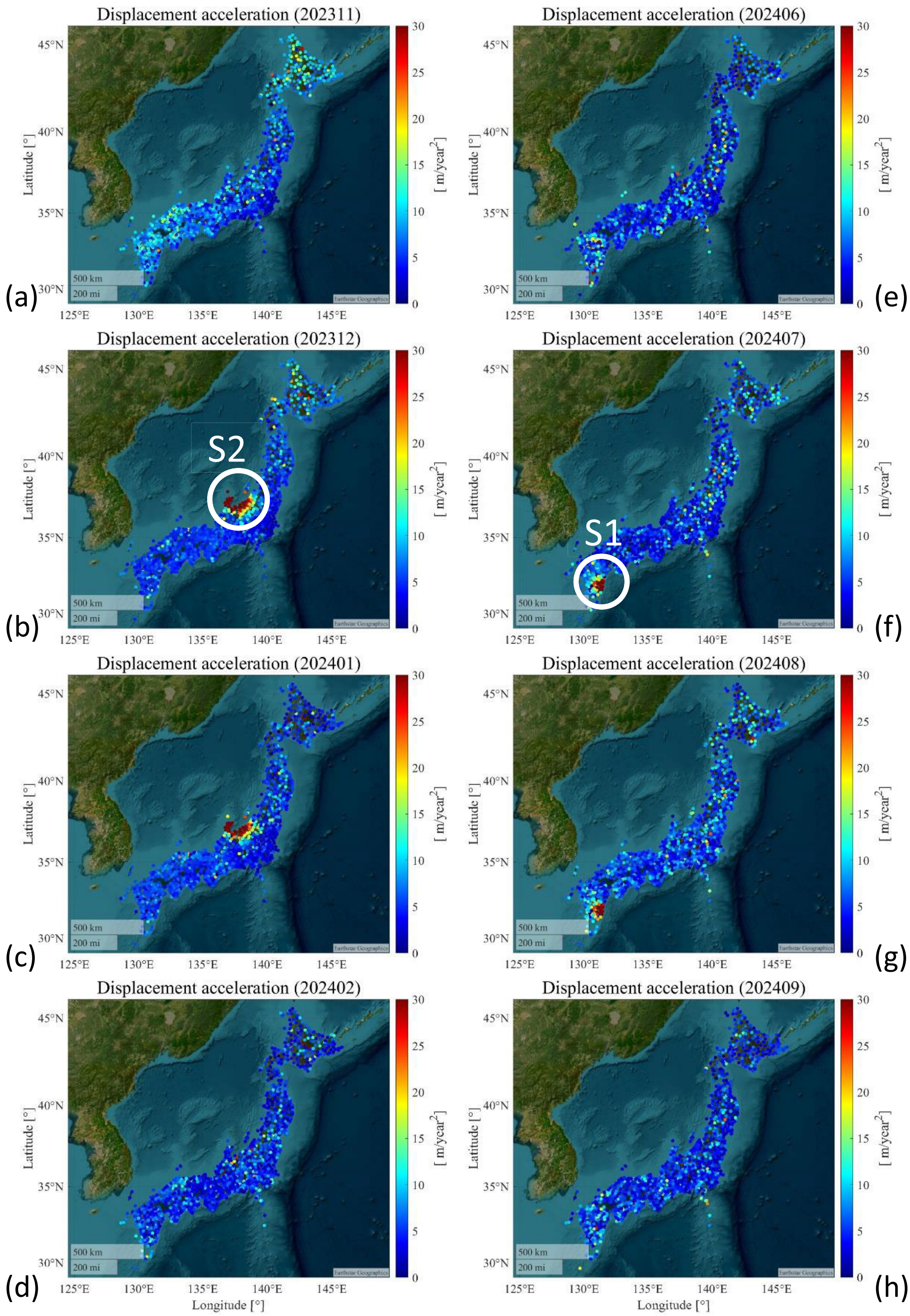

FIGURE 8. Sum of absolute derivative of velocities for each GNSS station. The velocities are based on a 15-d interval. The unit is [m/year2]. Results are obtained by using coordinates in (a) November 2023, (b) December 2023, (c) January 2024, (d) February 2024, (e) June 2024, (f) July 2024, (g) August 2024, and (h) September 2024. Large earthquakes occurred around S2 on January 1, 2024 and around S1 on August 8, 2024, respectively.

signs of the acceleration, but calculated the sum of the absolute derivatives of velocities because the sum of the signed derivatives could be close to zero as the positive and negative accelerations were canceled.

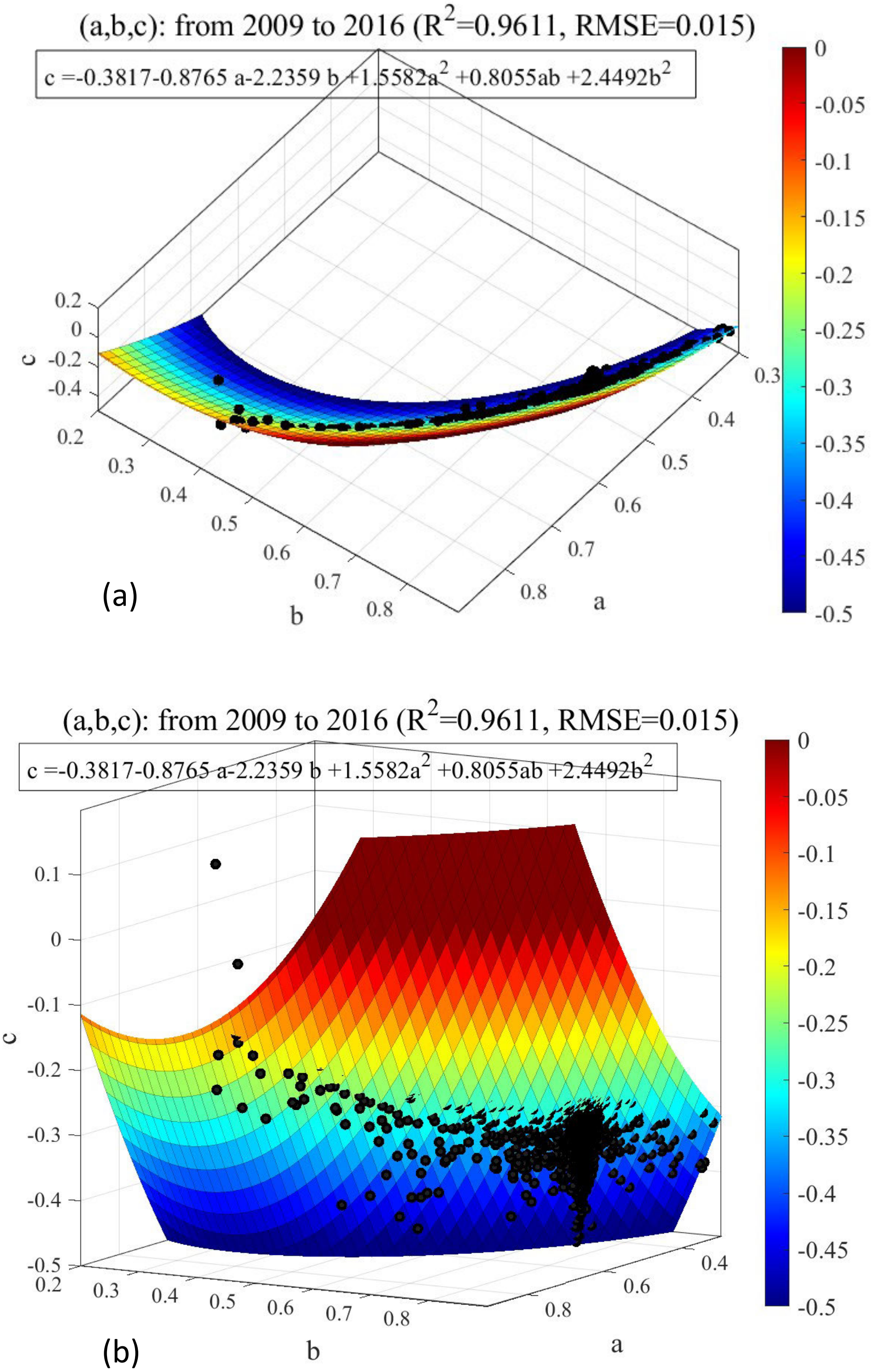

FIGURE 9. Curve surface fitting results. Results are obtained by fitting to (a,b) normal coefficients (a, b, c) obtained from the coordinates for 2009–2016. The coefficients of determination in curve surface fitting are 0.9611 for (a,b).

Monthly velocities and 15-d interval velocities were used for our analysis. We found that the results from the monthly velocities did not show a significant difference between years, but the results from the 15-d interval velocities showed many significant differences between years. In addition, we shortened the duration of the calculation from one year to one month. This one-month period was effective for understanding nationwide motions and local differences. The area that

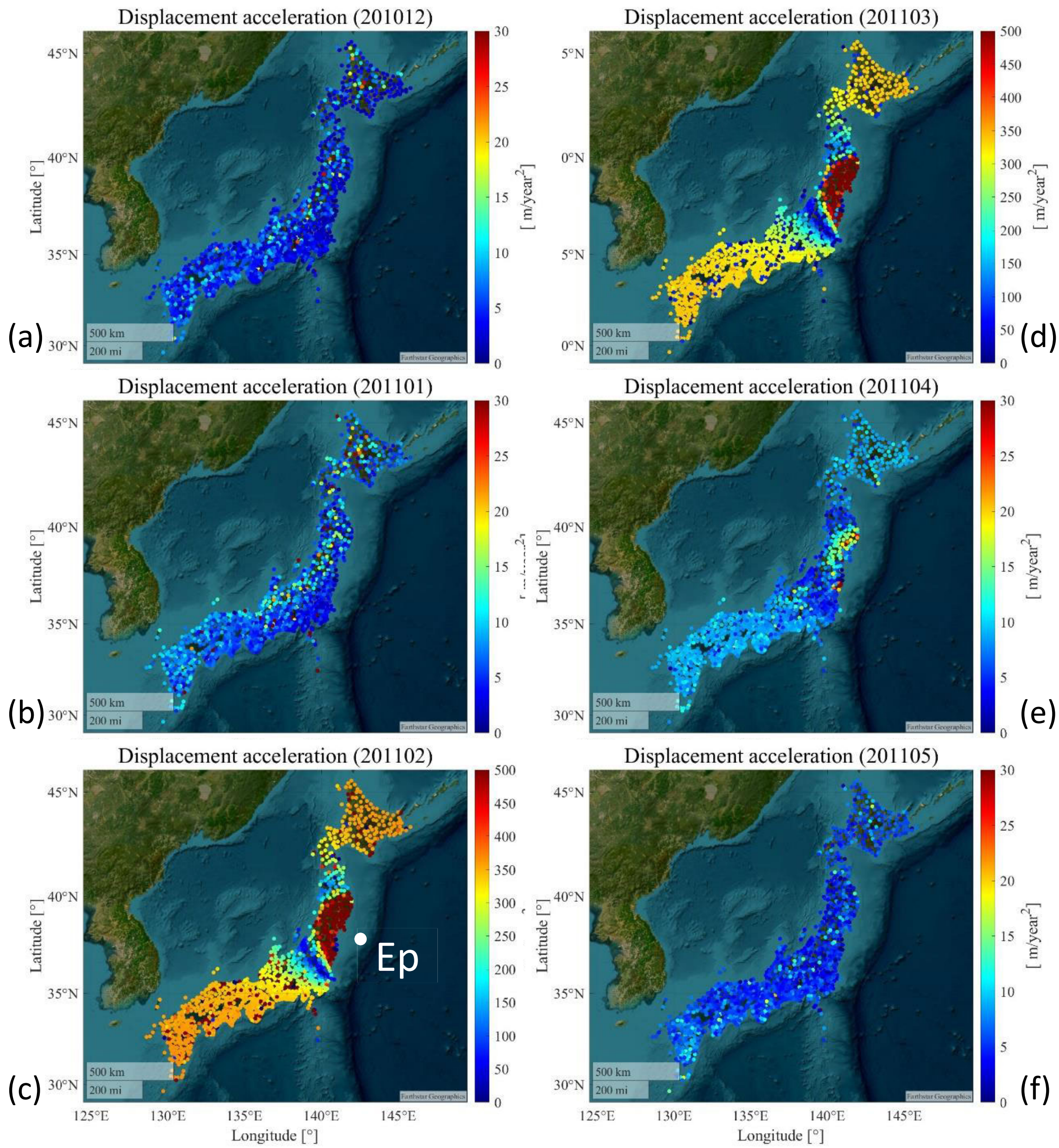

FIGURE 10. Sum of absolute derivative of velocities for each GNSS station. The velocities are based on a 15-d interval. The unit is [m/year2]. Results are obtained by using coordinates in (a) December 2010, (b) January 2011, (c) February 2011, (d) March 2011, (e) April 2011, and (f) May 2011. A large earthquake whose epicenter is expressed as "Ep" in (c) occurred on March 11, 2011.

includes Station 2, i.e., the Noto Peninsula, was damaged by two earthquakes that struck on May 5, 2023, and January 1, 2024. Active motion was observed in this area in December 2023 and January 2024, as shown in Figs. 8(b) and 8(c), respectively. However, a significant motion was not observed for the earthquake on May 5, 2023. Note that the monthly sum of absolute derivative were calculated from using 15-d interval velocities for the one and half month period. For example, 8(b) were calculated from the data from December 1, 2023 to January 16, 2024. In this regard, it is natural that Figs. 8(b) includes an active motion. We can not find such an active motion in Fig. 8(a). This means that the sum of the absolute derivatives of velocities is not a meaningful indicator to explain displacement before a significantly large earthquake occurs.

A similar trend was observed at Station 1. The area, including Station 1, was struck by an earthquake on August 8, 2024. In Figs 8(f) and 8(g), the area exhibited a much larger sum of absolute accelerations than those of other periods. Figures 8(f) and 8(g) used the data observed from July 1 to August 16, 2024, and that from August 1 to September 16, 2024, respectively. Another trend was observed in Area 1, shown in Fig. 3(a). On March 11, 2011, the Tohoku earthquake (Mj 9.0) struck off the Pacific coast.

Figures 10(c) and 10(d) show a significantly large sum of displacement accelerations in February 2011 and March 2011, respectively, whereas no significant trend was observed in the previous period, i.e., January 2011. As a result, we need a further investigation to find a more effective indicator for warning before a large earthquake.

V. CONCLUSION

We revealed that the displacement velocities of GNSS stations were on a planar surface both in each year and for several years. Although a significantly large displacement occurred, the displacement velocities remained close to those of the same planar surface. In addition, we found that the normal components (a, b, c) of the planar surfaces form a quadratic curve surface when we assumed the normal components as a point in the 3D coordinate system. The scattergrams repeated convergence and divergence periodically, but they seem on almost the same curve surface. We also examined the analysis to calculate the sum of absolute accelerations to explain displacement before a significantly large earthquake occurs. However, this indicator was not successful.

In future, we will develop an indicator to express warnings regarding large displacements. However, a limitation is that the geometric features shown in Figs. 6, 7(a), and 7(b) should be used further. We calculated the dot products of (a, b, c) obtained from the data for each year and (a, b, c) from the data for all years. We failed to derive a universal rule for earthquake forecasting that is applicable to all GNSS stations. In the future, we intend examining the formulation of a numerical index in the 3D coordinate system of (a, b, c).

REFERENCES

[1] H. Yamanaka, Y. Hiramatsu, and H. Katao, "Spatial distribution of atypical aftershocks of the 1995 hyogo-ken nanbu earthquake," *Earth, Planets Space*, vol. 54, no. 10, pp. 933–945, Jun. 2014, doi: 10.1186/bf03352441.

[2] V. N. Morozov and A. I. Manevich, "Mechanism of rupture formation of the Hanshin–Awaji earthquake (kobe, Japan) January 17, 1995, m 6.9," *Doklady Earth Sci.*, vol. 499, no. 2, pp. 654–660, Aug. 2021, doi: 10.1134/s1028334x21080080.

[3] K. Tamaribuchi, S. Kudo, K. Shimojo, and F. Hirose, "Detection of hidden earthquakes after the 2011 Tohoku earthquake by automatic hypocenter determination combined with machine learning," *Earth, Planets Space*, vol. 75, no. 1, p. 155, Oct. 2023, doi: 10.1186/s40623-023-01915-3.

[4] Geospatial Authority Jpn. (GSI). *Information About the 2024 Noto Peninsula Earthquake*. Accessed: Mar. 8, 2025. [Online]. Available: https://www.gsi.go.jp/BOUSAI/20240101_noto_earthquake.html

[5] Jpn. Meteorological Agency (JMA). *Information About the 2024 Noto Peninsula Earthquake*. Accessed: Mar. 8, 2025. [Online]. Available: https://www.jma.go.jp/jma/menu/20240101_noto_jishin.html

[6] A. Kato, S. Sakai, T. Iidaka, T. Iwasaki, E. Kurashimo, T. Igarashi, N. Hirata, and T. Kanazawa, "Group for the aftershock observations of the 2007 Noto hanto earthquake, three-dimensional velocity structure in the source region of the Noto hanto earthquake in 2007 imaged by a dense seismic observation," *Earth Planet Space*, vol. 60, pp. 105–110, Jul. 2008.

[7] A. Kato, "Implications of fault-valve behavior from immediate aftershocks following the 2023 Mj6.5 earthquake beneath the Noto peninsula, central Japan," *Geophys. Res. Lett.*, vol. 51, no. 1, Jan. 2024, Art. no. e2023GL106444.

[8] J. Nakajima, "Crustal structure beneath earthquake swarm in the Noto peninsula, Japan," *Earth, Planets Space*, vol. 74, no. 1, p. 160, Nov. 2022.

[9] T. Nishimura, Y. Hiramatsu, and Y. Ohta, "Episodic transient deformation revealed by the analysis of multiple GNSS networks in the Noto Peninsula, central Japan," *Sci. Rep.*, vol. 13, no. 1, p. 8381, Jun. 2023.

[10] Y. Ishikawa and L. Bai, "The 2024 mj 7.6 Noto Peninsula, Japan earthquake caused by the fluid flow in the crust," *Earthq. Res. Adv.*, vol. 4, no. 3, Jul. 2024, Art. no. 100292.

[11] A. Ferretti, C. Prati, and F. Rocca, "Permanent scatterers in SAR interferometry," *IEEE Trans. Geosci. Remote Sens.*, vol. 39, no. 1, pp. 8–20, Jan. 2001.

[12] P. Berardino, G. Fornaro, R. Lanari, and E. Sansosti, "A new algorithm for surface deformation monitoring based on small baseline differential SAR interferograms," *IEEE Trans. Geosci. Remote Sens.*, vol. 40, no. 11, pp. 2375–2383, Nov. 2002.

[13] A. Ferretti, A. Fumagalli, F. Novali, C. Prati, F. Rocca, and A. Rucci, "A new algorithm for processing interferometric data-stacks: SqueeSAR," *IEEE Trans. Geosci. Remote Sens.*, vol. 49, no. 9, pp. 3460–3470, Sep. 2011.

[14] E. Chaussard, S. Wdowinski, E. Cabral-Cano, and F. Amelung, "Land subsidence in central Mexico detected by ALOS InSAR time-series," *Remote Sens. Environ.*, vol. 140, pp. 94–106, Jan. 2014.

[15] S. Fujiwara, T. Nishimura, M. Murakami, H. Nakagawa, M. Tobita, and P. A. Rosen, "2.5D surface deformation of M6.1 earthquake near mt Iwate detected by SAR interferometry," *Geophys. Res. Lett.*, vol. 27, no. 14, pp. 2049–2052, Jul. 2000.

[16] J. Huang, T. Xia, Y. Shuai, and H. Zhu, "Assessing the performance of GEDI LiDAR data for estimating terrain in densely forested areas," *IEEE Geosci. Remote Sens. Lett.*, vol. 20, pp. 1–5, 2023, doi: 10.1109/LGRS.2023.3306875.

[17] D. Sakaizawa, Y. Okawa, R. Mitsuhashi, Y. Sawada, T. Imai, and T. Sumita, "Research and development for the ISS-based LiDAR mission moli," in *Proc. IEEE Int. Geosci. Remote Sens. Symp. (IGARSS)*, Jul. 2024, pp. 937–940, doi: 10.1109/IGARSS53475.2024.10642232.

[18] *EoPortal, ISS: GEDI (Global Ecosystems Dynamics Investigation LiDAR)*. Accessed: Mar. 8, 2025. [Online]. Available: https://www.eoportal.org/satellite-missions/iss-gedi#mission-capabilities

[19] N. T. Kurtz, T. Markus, D. J. Cavalieri, W. Krabill, J. G. Sonntag, and J. Miller, "Comparison of ICESat data with airborne laser altimeter measurements over Arctic sea ice," *IEEE Trans. Geosci. Remote Sens.*, vol. 46, no. 7, pp. 1913–1924, Jul. 2008, doi: 10.1109/TGRS.2008.916639.

[20] L. A. Magruder and K. M. Brunt, "Performance analysis of airborne photon-counting LiDAR data in preparation for the ICESat-2 mission," *IEEE Trans. Geosci. Remote Sens.*, vol. 56, no. 5, pp. 2911–2918, May 2018, doi: 10.1109/TGRS.2017.2786659.

[21] P. Rebischung, Z. Altamimi, L. Métivier, X. Collilieux, K. Gobron, and K. Chanard, "Analysis of the IGS contribution to ITRF2020," *J. Geodesy*, vol. 98, no. 6, p. 49, Jun. 2024, doi: 10.1007/s00190-024-01870-1.

[22] *NOAA CORS Network—National Geodetic Survey*. Accessed: Mar. 8, 2025. [Online]. Available: https://geodesy.noaa.gov/CORS/

[23] C. Bruyninx, J. Legrand, A. Fabian, and E. Pottiaux, "GNSS metadata and data validation in the EUREF permanent network," *GPS Solutions*, vol. 23, no. 4, p. 106, Oct. 2019, doi: 10.1007/s10291-019-0880-9.

[24] *EUREF Permanent GNSS Network*. Accessed: Mar. 8, 2025. [Online]. Available: https://www.epncb.oma.be/

[25] *Network of GNSS Permanent Stations of Spain (ERGNSS)*. Accessed: Mar. 8, 2025. [Online]. Available: https://data.europa.eu/data/datasets/spaignredergnss?locale=en

[26] M. Ramatschi, M. Bradke, T. Nischan, and B. Männel, "GNSS data of the global GFZ tracking network. V. 1," GFZ Data Services, Germany, Tech. Rep., 2019, doi: 10.5880/GFZ.1.1.2020.001.

[27] H. Tsuji and Y. Hatanaka, "GEONET as infrastructure for disaster mitigation," *J. Disaster Res.*, vol. 13, no. 3, pp. 424–432, Jun. 2018, doi: 10.20965/jdr.2018.p0424.

[28] S. Kawamoto, N. Takamatsu, and S. Abe, "RINGO: A RINEX preprocessing software for multi-GNSS data," *Earth, Planets Space*, vol. 75, no. 1, p. 54, Apr. 2023, doi: 10.1186/s40623-023-01811-w.

[29] K. Ohno, Y. Ohta, S. Kawamoto, S. Abe, R. Hino, S. Koshimura, A. Musa, and H. Kobayashi, "Real-time automatic uncertainty estimation of coseismic single rectangular fault model using GNSS data," *Earth, Planets Space*, vol. 73, no. 1, p. 127, Dec. 2021, doi: 10.1186/s40623-021-01425-0.

[30] K. Ohno, Y. Ohta, R. Hino, S. Koshimura, A. Musa, T. Abe, and H. Kobayashi, "Rapid and quantitative uncertainty estimation of coseismic slip distribution for large interplate earthquakes using real-time GNSS data and its application to tsunami inundation prediction," *Earth, Planets Space*, vol. 74, no. 1, p. 24, Dec. 2022, doi: 10.1186/s40623-022-01586-6.

[31] K. Ohno, Y. Ohta, N. Takamatsu, H. Munekane, and M. Iguchi, ''Real-time modeling of transient crustal deformation through the quantification of uncertainty deduced from GNSS data,'' *Earth, Planets Space*, vol. 76, no. 1, p. 140, Nov. 2024, doi: 10.1186/s40623-024-02068-7.

[32] N. Takamatsu, H. Muramatsu, S. Abe, Y. Hatanaka, T. Furuya, Y. Kakiage, K. Ohashi, C. Kato, K. Ohno, and S. Kawamoto, ''New GEONET analysis strategy at GSI: Daily coordinates of over 1300 GNSS CORS in Japan throughout the last quarter century,'' *Earth, Planets Space*, vol. 75, no. 1, p. 49, Apr. 2023, doi: 10.1186/s40623-023-01787-7.

[33] G.-Q. Shi, X.-F. He, and R.-Y. Xiao, ''Acquiring three-dimensional deformation of Kilauea's south flank from GPS and DInSAR integration based on the ant colony optimization,'' *IEEE Geosci. Remote Sens. Lett.*, vol. 12, no. 12, pp. 2506–2510, Dec. 2015.

[34] H. Ito, J. Susaki, and T. Anahara, ''Integrating multi-temporal SAR images and GPS data to monitor three-dimensional land subsidence,'' *ISPRS Ann. Photogramm., Remote Sens. Spatial Inf. Sci.*, vol. 3, pp. 9–16, Mar. 2019.

[35] S. Gudmundsson, F. Sigmundsson, and J. M. Carstensen, ''Three-dimensional surface motion maps estimated from combined interferometric synthetic aperture radar and GPS data,'' *J. Geophys. Res., Solid Earth*, vol. 107, no. B10, pp. 2250–2264, Oct. 2002.

[36] J. Susaki, T. Kusakabe, and T. Anahara, ''Estimating 3D land subsidence from multi-temporal SAR images and GNSS data using weighted least squares,'' *ISPRS Ann. Photogramm., Remote Sens. Spatial Inf. Sci.*, vol. 3, pp. 165–172, Aug. 2020.

[37] J. Susaki and Y. Teranishi, ''Unbiased estimation of three-dimensional deformation from SAR interferometry and GNSS observations,'' *IEEE J. Sel. Topics Appl. Earth Observ. Remote Sens.*, vol. 17, pp. 5761–5773, 2024.

[38] GSI. *Daily Geolocational Data of GNSS Stations*. Accessed: Mar. 8, 2025. [Online]. Available: https://terras.gsi.go.jp/pos_main.php

JUNICHI SUSAKI (Senior Member, IEEE) received the B.E., M.E., and D.Eng. degrees in civil engineering from The University of Tokyo, Tokyo, Japan, in 1995, 1997, and 2000, respectively. He has been an Associate Professor and a Professor with Kyoto University, Kyoto, Japan, since 2007 and 2020, respectively. His current research interests include urban monitoring and modeling using SAR, optical sensors, and LiDAR for applications, such as disaster mitigation and environmental change analysis.